Evaluation of scanning transmission X-ray microscopy at the Mn L2,3-edges as a potential probe for manganese redox state in natural silicates

Franck Bourdelle, Emily Lloret, Cyril Durand, Laura Airaghi

Title: **Evaluation of scanning transmission X-ray microscopy at the Mn $L_{2,3}$-edges as a potential probe for manganese redox state in natural silicates**

Authors: Franck Bourdelle[a,*], Emily Lloret[a], Cyril Durand[a], Laura Airaghi[b]

Affiliations:

[a] Univ. Lille, Institut Mines-Télécom, Univ. Artois, Junia, ULR 4515 - LGCgE, Laboratoire de Génie Civil et géo-Environnement, F-59000 Lille, France

[b] University of Orléans, CNRS, BRGM, ISTO, UMR 7327, F-45071, Orléans, France

*Corresponding authors:

Dr. Franck Bourdelle

Present mailing address: Laboratoire Génie Civil et géo-Environnement (LGCgE) – Département des Sciences de la Terre, Université de Lille, Cité Scientifique, Bâtiment SN5, 59655 Villeneuve d'Ascq Cedex, France.

E-mail address: franck.bourdelle@univ-lille.fr

Phone number: + 33 (0)3 20 43 41 13

ORCID:

Franck Bourdelle: 0000-0002-7136-8692

Emily Lloret: 0000-0003-0952-9202

Cyril Durand: 0000-0001-8341-8450

Laura Airaghi: 0000-0001-7032-2732

Abstract

Determining the Mn valence variation at the nanometer scale will be an important advance in the study of heterogeneous natural silicates. Here, the potential of the scanning transmission X-ray microscopy at the Mn $L_{2,3}$-edges (640 - 655 eV) as a probe for manganese redox state is evaluated. For this purpose, several natural Mn-silicates (rhodonite, ardennite, piemontite, Mn^{4+}-silicate, jacobsite), covering several Mn valence, were analysed to identify the spectral parameters most sensitive to the Mn valence, regardless of the coordination environment, the crystal field strength, the nature and the length of the metal–ligand bonds, and the intra-atomic Coulomb and spin–orbit interactions. Two suitable spectral empirical calibrations are thus proposed, linking the Mn valence to two peak intensity ratios: one ratio of intensities from two energy points of the L_2 peak (at 651.7 and 655.2 eV), and one ratio of intensities from one energy point of the L_2 peak (at 655.2 eV) and one of the L_3 peak (at 641.6 eV). Thank to them, the first quantitative Mn valence maps are constructed, with a high spatial resolution (< 40 nm pixel size), opening the way to exhaustive crystallochemical studies of silicates containing Mn with different valences.

Key words: manganese valence; STXM; XANES spectroscopy; $L_{2,3}$-edges; redox mapping; silicates

Declarations

Funding: This study was financially supported by LGCgE (laboratory funds).

Conflicts of interest/Competing interests: Not applicable.

Availability of data and material: XANES spectra are available on request from franck.bourdelle@univ-lille.fr

Code availability: Not applicable.

Authors' contributions (optional): -

1. Introduction

Constraining redox conditions during sediment deposition, rock formation or mineralogical transformation is of primary importance to understand the P-T-X history (pressure-temperature-composition) of geological systems. Redox conditions are usually assessed by the analysis of minerals since they partly influence their chemical composition. The evaluation of redox conditions is often based on the iron redox state, i.e. by the quantification of the Fe^{3+}/Fe^{2+} ratio in minerals – mainly silicates, major constituents of crusts – when they can contain both divalent and trivalent cations (i.e. Inoue et al. 2018). More rarely, the redox state of other metals is investigated, as manganese. However, Mn – which can be present as Mn^{2+}, Mn^{3+} and sometimes-but-rarely Mn^{4+} – could be a good indicator of paleo-conditions of rock formation (Loomer et al. 2007), even if Mn-silicates, specially P-T-X sensitive silicate solid solution such as phyllosilicates, are infrequent, at the very least not ubiquitous in sedimentary and metamorphic rocks, and that the Mn content of these silicates is low. In this way, Sussenberger et al. (2018) suggest that Mn content in chlorite could be a proxy for chemo-stratigraphic conditions in depositional environment. For their part, Bobos et al. (2018) establish a link between Mn-chlorite and Wolframite, the Mn content in chlorite becoming an indicator of W-Mo mineralisation.

Unfortunately, authors could not determine the Mn^{3+}/Mn^{2+} ratio which would have noticeably modified the chlorite structural formula calculation, and potentially the subsequent interpretations. In the past, different techniques have been envisaged for this purpose, including electron microprobe analysis (EMPA, e.g. Albee and Chodos 1970), X-ray photoelectron spectroscopy (XPS, e.g., Ilton et al. 2016) or X-ray absorption near edge structure (XANES) spectroscopy at the K-edge (e.g. Manceau and Gallup 2005; Manceau et al. 2012). However, none of these methods provides a nanometer-scale spatial resolution, which could be particularly useful to identify chemical and redox zonation patterns in low-temperature crystals (e.g. Bourdelle et al. 2018). On the other hand, several studies (e.g., Garvie and Craven 1994; van Aken and Liebscher 2002) have shown that electron energy-loss

spectroscopy (EELS) carried out in a transmission electron microscope (TEM) is a powerful method for determining the redox state of transition metals at a submicrometric resolution, including Mn in silicates, but sometimes induces severe beam damage effects, such as electron beam-induced reduction of manganese (Lauterbach et al. 2000; de Groot et al. 2010; Livi et al. 2012). The XANES spectroscopy at the $L_{2,3}$-edges is often proposed as a powerful alternative and is increasingly used in the Earth sciences. Firstly, the X-ray energies required for XANES analysis are lower at the $L_{2,3}$-edges (between ~640 and 655 eV) than at the K-edge (between ~6500 and 6580 eV), allowing higher resolutions, i.e. < 0.1 eV and ~30 nm at existing synchrotron facilities. Secondly, the X-ray incident beam is less destructive for samples than the TEM-EELS electron beam.

The XANES spectroscopy at the $L_{2,3}$-edges is based on the $2p \rightarrow 3d$ electronic transition, which is sensitive to – among other parameters – the metal valence (e.g. Garvie and Craven 1994). De Groot et al. (1994) describing in detail the complex physical basis of Mn $L_{2,3}$-edges, underlined that Mn valence can be obtained from $L_{2,3}$-edge spectra by a multiplet calculation. However, this approach remains difficult to use in the case of natural minerals whose structure has not been beforehand determined. Otherwise, the Mn valence can be evaluated by fitting $L_{2,3}$-edge spectra with a combination of reference spectra, but this requires Mn^{2+}, Mn^{3+}, Mn^{4+} reference compounds, with Mn in the same local coordination environment than the studied sample. Consequently, several authors have turned to empirical approaches, trying to find a spectral parameter depending only (or at least, mainly) on the Mn valence. The white-line ratio, calibrated by van Aken and Liebscher (2002), is probably the best known, linking the formal transition metal valence to the ratio of integral intensity (over a 2 eV window) of the L_3 and L_2 excitation peaks. Recently, Wang et al. (2018) used the integrated L-edge intensity, considering it is proportional to the total number of *3d* holes localized in the X-ray absorber (normalized to this invariant edge jump), while Risch et al. (2017) proposed a linear correlation between Mn valence and the energy of the center of gravity of the Mn L_3-edge. But these methods, a review of which was proposed by Tan et al.

(2013), were often calibrated for Mn-oxides, but were not tested on Mn-silicates, which present specific structures.

Moreover, synchrotron facilities make possible to carry out Mn $L_{2,3}$-edge XANES spectroscopy with a scanning transmission X-ray microscope (STXM), one spectrum being one image pixel of the studied sample area (e.g. Bourdelle et al. 2013). This makes it possible to consider extracting quantitative maps of Mn valence over the entire area of interest, very useful for heterogeneous natural samples containing mixed oxidation state Mn species. Pecher et al. (2003) explore the feasibility of such maps extracted from STXM-XANES data, in order to characterize the Mn charge state distribution in biominerals. Unfortunately, in absence of empirical calibration based on a spectral intensity ratio rather than an integrated area or a center of gravity calculation, the resulting maps remain qualitative.

From these observations, we want to evaluate the potential of the scanning transmission X-ray microscopy at the Mn $L_{2,3}$-edges as a probe for manganese redox state investigations in natural silicates, defining a suitable spectral empirical calibration allowing to construct quantitative Mn valence maps with a high spatial resolution (nanoscale).

2. Materials and methods

2.1. Natural samples

Samples used in this study were natural silicates, containing various Mn amount and covering the three common Mn redox state (2+, 3+, 4+). As the shape of the Mn $L_{2,3}$-edge spectra can be influenced by, among others parameters, the Mn coordination, one oxide presenting Mn in tetrahedral coordination sites is also considered. Particles transparent to soft X-rays are needed to measure XANES spectra in the transmission mode of STXM, therefore samples are prepared as grounded powders dispersing in ethanol; a drop of which is placed (then evaporated) on a carbon holey support film placed on a 200 mesh copper grid.

The selected silicates are rhodonite, ardennite, piemontite and a Mn^{4+}-silicate (Table 1), for which chemical composition has been verified by Energy-dispersive X-ray

spectroscopy, the EDX probe being coupled to a Scanning electron microscopy (QUANTA 200 SEM instrument operating at 15 kV with a 1.5 nA current; mineral standards used for EDX probe calibration: albite, diopside, orthoclase, garnet and $MnTiO_3$; ZAF correction applied). Rhodonite is a Mn^{2+} pyroxenoid, where Mn is mainly in 6 coordination, sometimes in 7 (Smyth and Bish 1988; Nelson and Griffen 2005). Mn is therefore in distorted octahedral sites, defined by Mn-O bonds. The rhodonite sample used here, whose formula is $Ca_{0.15}Mn_{0.85}SiO_3$, comes from Gambaseta (Liguria, Italia). Ardennite is a Mn^{2+} sorosilicate described by the following formula: $Mn_4Al_4(AlMg)(AsO_4)(SiO_4)_2(Si_3O_{10})(OH)_6$. In it, Mn is located in large polyhedron, based on 5 coordination via Mn-O bonds, and 2 additional coordination via Mn-OH bonds (Donnay and Allmann 1968). Here, one specimen of As-Ardennite from Salm-Château (Ardennes, Belgium) was studied; the composition does not present an excess of Mn (< 4 atoms per formula unit), all Mn is consequently assumed as Mn^{2+} (Nagashima and Armbruster 2020). Piemontite is a Mn-rich epidote, where Mn is in trivalent form and occupies octahedral sites. The selected specimen comes from the Prabornaz mine (Aosta, Italia), with the verified chemical formula $Ca_{2.05}(Al_{1.68}Fe^{3+}_{0.49}Mn^{3+}_{0.83})(Si_{2.0}O_7)(Si_{1.0}O_4)O(OH)$. The last studied Mn-silicate, a rare type of silicates that contains tetravalent Mn similarly to stavelotite-(La), was sampled at Eveslogchorr (Murmansk Oblast, Russia) combined with pectolite and has the determined empirical formula: $Na_{0.3}Ca_{1.4}Fe^{3+}_{0.3}Mn^{4+}_5SiO_{14}$. A jacobsite sample, from Langban, (Filipstad, Sweden), was also analysed. Jacobsite is an Mn^{2+} oxide belonging to the spinel group, with the common formula $MnFe_2O_4$. As a "normal spinel", Mn^{2+} occupies tetrahedral sites formed by 4 oxygens (Bosi et al. 2019).

Table 1: Samples used for STXM-XANES Mn $L_{2,3}$-edge investigations to Mn mean valence quantification

Type	Sample	Location	Mn valence	Position of major peaks (eV)	
				L_3	L_2
Silicate	Rhodonite	Gambaseta (Liguria, Italia)	2+	641.6	654.1

Silicate	Ardennite	Salm-Château (Ardennes, Belgium)	2+	641.6	654.1
Silicate	Piemontite	Prabornaz mine (Aosta, Italia)	3+	643.2	654.4
Silicate	Mn^{4+}-silicate	Eveslogchorr (Murmansk Oblast, Russia)	4+	644.6	655.2
Oxide	Jacobsite	Langban (Filipstad, Sweden)	2+	641.6	654.1

2.2. STXM and XANES spectroscopy

The STXM is able to record the transmitted soft X-ray intensity on each point of the pluri-micrometric-sized area of interest for each defined energy. Therefore, STXM gives 2D images for which each pixel represents a soft X-ray absorption spectrum. This is of great interest for mapping metal oxidation state variation into small crystallites (e.g. Bourdelle et al. 2013). In the present study, STXM analyses were acquired on the PolLux beamline at the Swiss Light Source (SLS, Villigen, Switzerland). The characteristics of the beamline are detailed by Raabe et al. (2008); the beam was in circular-polarisation configuration to avoid crystal lattice orientation dependency of analysis (see below). The scanning transmission X-ray microspectroscopy endstation allows to achieve stacks and linescans, i.e. a spectral map of an area and a sum of spectra for each pixel of a line, respectively. Stacks were recorded over the 635–660 eV energy range (Mn $L_{2,3}$-edge) using a 0.2 eV spectral resolution and a 40 nm spatial resolution. Linescans were recorded over the same energy range, using a 0.1 eV spectral resolution. The dwell time per image- and energy- point was between 1 and 10 ms. Focus was checked systematically for each particle. STXM-XANES data were post-processed using the aXis2000 software (Hitchcock 2012). Beam damages caused by the incident beam were assessed by monitoring spectral changes at the Mn $L_{2,3}$-edges with increasing dwell times up to 20 ms.

2.3. Spectrum processing

Spectra were extracted from stacks and linescans in form of optical density spectra (noted OD), obtained as $OD = -ln(I/I_0)$, where I is the X-ray intensity transmitted from the sample, and I_0 is those recorded without samples. Then two steps of processing were applied on spectra:

(i) a linear background correction was applied to remove the contribution of lower energy absorption edges, so that the pre-edge region is set to 0 optical density.

(ii) the two edge steps resulting from transitions to unoccupied states in the continuum were subtracted using a double arctan function (Chen et al. 1995; van Aken and Liebscher 2002; Brotton et al. 2007) as:

$$f(\Delta E) = \frac{h_1}{\pi}\left(\tan^{-1}\left[\frac{\pi}{w_1}(\Delta E - E_1)\right] + \frac{\pi}{2}\right) + \frac{h_2}{\pi}\left(\tan^{-1}\left[\frac{\pi}{w_2}(\Delta E - E_2)\right] + \frac{\pi}{2}\right) \quad (1)$$

where h_1 and h_2 are the step heights of the two arctan functions, w_1 and w_2 are fixed peak widths and E_1 and E_2 are the positions of the inflection points resulting in an energy near the edge onset. Brotton et al. (2007) proposed setting the function slope w at 5 eV, to account for the slow onset of the continuum. Following this recommendation, w_1 and w_2 were fixed to 5 eV. For each sample, four or five spectra on different particles were extracted to evaluate the spectral variability. A total of 23 spectra were thus used in this study.

3. Results and discussion

3.1. Influences of Mn redox state, coordination and atomic environment on the shape of Mn $L_{2,3}$-edge XANES spectrum

X-ray absorption near edge structure spectra at the Mn $L_{2,3}$-edges for Mn-silicates and jacobsite are shown in Figure 1, where peaks are identified by letters (from L_3-a to L_3-h and from L_2-a to L_2-e) and linear background is subtracted. These spectra result from transitions from *2p* core electrons to *3d* state, *4s* state or continuum as follow:

- two strong absorption peaks, usually noted L_3 and L_2, due to the spin-orbit splitting of *2p* level (van Aken and Liebscher 2002; Nishida et al. 2013) involving transitions from $2p_{3/2}$ and $2p_{1/2}$ states to empty *3d* atomic orbitals, respectively. From a $2p^6 3d^n$ ground state, the absorption process leads to a core-excited $2p^5 d^{n+1}$ final state, as $3d^5$ for Mn^{2+}, $3d^4$ for Mn^{3+} and $3d^3$ for Mn^{4+}, implying variations in absorption energy.

- edge jump steps at the bottom of L_3 and L_2 peaks, corresponding to *2p* → continuum transitions.
- negligible contributions of *2p* → *4s* transitions, which are 20 times weaker in intensity than *2p* → *3d* transitions.

Each L_3 and L_2 peak consists of one major peak accompanied on both sides by several minor peaks. The energy position of these major peaks mainly depends (but not only) on the core-excited final state, i.e. Mn redox state: 641.6 and 654.1 eV for Mn^{2+} (L_3-b and L_2-c, respectively; rhodonite, ardennite, jacobsite), 643.2 and 654.4 eV for Mn^{3+} (L_3-e and L_2-d, respectively; piemontite), 644.6 and 655.2 eV for Mn^{4+} (L_3-f and L_2-e, respectively; Mn^{4+}-silicate). In this way, spectra are qualitatively similar to those described in several previous studies, obtained using different analytical techniques (e.g. Garvie and Craven 1994; Morales et al. 2004; Zhang et al. 2010; Kubin et al. 2018).

Minor peaks arise from factors other than redox as their number, intensity and shape vary from one sample to another. Therefore, Mn^{2+} spectra present 3 minor peaks (L_3-a, L_3-d and L_3-g with a shoulder peak noted L_3-h) around L_3-b, and 2 minor peaks (L_2-a, L_2-b) before L_2-c, more intensive (related to the intensity of major peaks) for rhodonite than for ardennite. Mn^{3+} and Mn^{4+} spectra have fewer minor peaks: only two, at the same (or very close) energy position than the L_3 and L_2 Mn^{2+} major peaks, and one more at 642.3 eV (L_3-c) only for Mn^{4+} spectra. These minor peaks are also observed in previous studies (e.g. de Groot et al. 2010; Cuartero et al. 2016; Risch et al. 2017), especially on Mn-oxide spectra, and are influenced by the Mn valence and coordination environment, the crystal field strength, the nature and the length of the metal–ligand bonds, and the intra-atomic *3d-3d* and *2p-3d* Coulomb and spin–orbit interactions in the *2p* core and *3d* orbitals.

Here, no complex calculations or multiplet analyses were used to describe spectrum shape in detail as the aim of the present study is to propose an easy-to-use approach to empirically map the Mn valence in silicates. However, some comments can be made to explain (i) the general shape of the Mn-silicate spectra and (ii) the great similarity of them with Mn-oxide spectra.

In fact, *3d* orbitals consist of five *d* orbitals, as three have lobes between x, y, z-axis (noted dxy, dxz, dyz) and two have lobes on the axes (noted dz^2 and dx^2-y^2). In octahedral coordination site, the 6 ligands approach Mn along the axes, increasing by electrostatic repulsion the energy of dz^2 and dx^2-y^2 orbitals (called e_g). Conversely, dxy, dxz, dyz orbitals (called t_{2g}) point between the ligands, that lowered their energies. This difference of energy between e_g and t_{2g} orbital groups defines the crystal field strength (Δ_o or 10Dq) (Burns 1993). In the case of 6 coordinated Mn^{2+}, the t_{2g} spectral contribution is often assigned to the L_3-a minor peak, while e_g is associated to the L_3-b major peak (Garvie and Craven 1994; de Groot et al. 1994), 10Dq can be deducting from the energy distance between these two peaks. In the Figure 2, focused on the L_3-edge part of Mn^{2+} absorption spectra (edge jump steps were subtracted), the energy gap between L_3-a and L_3-b is very weak (< 1 eV), suggesting a low 10Dq value. The comparison with 10Dq calculations and estimates from experiments previously published (Garvie and Craven 1994; Garvie et al. 1994; Pérez-Dieste et al. 2004) confirms that 10Dq value is probably around 0.5 or 1 eV. The energy difference between t_{2g} and e_g orbital groups remains therefore weak enough for Mn to be in high-spin state (Burns 1993), which is the most common spin configuration for Mn (Garvie and Craven 1994; de Groot 1994). The Figure 2 also shows that the energy position of L_3-a is always the same whatever the Mn^{2+} mineral studied in our conditions, but that its intensity (related to L_3-b major peak intensity) is variable. This observation is also suitable for other minor peaks L_3-d and L_3-g, suggesting the contribution of another significant factors. In fact, Mn^{2+} in rhodonite, ardennite and jacobsite is located in different coordination sites, with different Mn-ligand bond length and different type of ligands. In rhodonite, Mn^{2+} occupies octahedral sites slightly distorted, elongated, due to the global structure, linked to 6 O (Smyth and Bish 1988). This configuration leads to an energy splitting between dx^2-y^2 and dz^2 orbitals ($E_{dx^2-y^2} > E_{dz^2}$) on the one hand, and between dxy and dxz, dyz orbitals ($E_{dxy} > E_{dxz}$ and E_{dyz}) on the other hand. In ardennite, Mn^{2+} is located in large polyhedron with a 6 or 7 coordination configuration, with O and OH as ligands (Donnay and Allmann 1968), also implying a substantial change in

orbital energies. In jacobsite, Mn^{2+} is surrounded by 4 O in a tetrahedral site. But in this case, the 4 ligands are closer to the dxy, dxz, dyz orbitals (t_2) than to the dz^2, dx^2-y^2 orbitals (e), leading to an inversion of the splitting energy, t_2 orbital group having higher energy than e orbital group (Burns 1993). Differences in spectrum shapes, especially the intensities of t_{2g} or t_g – L_3-a (virtually disappeared in the case of jacobsite), L_3-d and L_3-g peaks, must be related to the coordination and the ligands of Mn. From an empirical point of view, the intensity of minor peaks decreases proportionally to the number of Mn-O bonds. On the other hand, the similarity of Mn-silicates (i.e. Mn^{2+}, Mn^{3+} and Mn^{4+} -silicates) and Mn-oxides spectra (from this study and literature) tends to indicate that, as a first approximation, the extended atomic environment (i.e. beyond the coordination site receiving Mn) has negligible influence compared to that of the near coordination.

Consequently, an empirical calibration linking a spectral parameter to the Mn mean valence must be mainly based on major peaks, most sensitive to redox, without taking into account an energy window (as white line ratio method) that might include minor peaks, most sensitive to the Mn coordination and the surrounding atomic environment. An empirical calibration is possible especially since the 10Dq is weak (van der Laan and Kirkman 1992).

3.2. Mn redox state estimation from $L_{2,3}$-edge XANES spectra

As three valence states of Mn could be present in silicates, it is not possible to determine easily, directly and empirically the relative proportion of each of them. As an alternative, XANES spectra allow to assess the Mn mean valence which, coupled to a structural formula obtained with an independent method, gives a strong indication of the likely $xMn^{2+} + yMn^{3+} + zMn^{4+}$ combination.

As referenced in the Figure 1, the main variation in the XANES spectra of silicates with the Mn valence involves the energy position of the L_3 major peak. More precisely, the L_3 major peak shifts to higher energies with increasing Mn charge, by a step of 1.4-1.6 eV. However, because this step and Mn valence are not linearly linked, Risch et al. (2017) prefer

to use the center of gravity of the L_3-edge. From Mn-oxides, authors propose a linear correlation implying to take in consideration the L_3 minor peaks in addition to major peaks. A such correlation was established here for silicates (Figure 3), and demonstrates the influence of minor peaks, i.e. of the type of coordination sites in which Mn occurs. Considering only the mineral phases where Mn occupies octahedral sites (piemontite, rhodonite) and Mn^{4+}-silicate, the relationship between nominal Mn valence and the L_3 center of gravity is linear, with a R^2 = 1. However, taking into account the ardennite in which Mn occupies large polyhedron or jacobsite in which Mn is in tetrahedral sites, the energy position of the L_3 center of gravity for Mn^{2+} phases depends on L_3-a, L_3-d and L_3-g peak weight and not only of Mn redox state. Mainly, the L_3 center of gravity is a spectral parameter including a peak area, not extractable from a stack. This approach therefore does not allow to easily map the Mn valence from STXM-XANES data.

In order to construct a redox map, it becomes therefore necessary to propose a new purely-empirical calibration of Mn valence with a simple spectral parameter, using selected energy points (and not a spectral surface as white line ratio or center of gravity), that does not need to have any physical significance (as an intensity ratio). Considering only the silicates (jacobsite is excluded) and the 13 identified peaks (Figure 1), 78 ratios of two peak intensities can be calculated, plus their inverses, namely 156 possibilities. But only 12 peak intensity ratios are in correlation with the Mn valence with a coefficient of determination higher than 0.98. In fact, the R^2 is very poor for intensity ratios implying major peaks of Mn^{3+} and minor peaks of Mn^{2+} (Figure 2). On the 12 peak intensity ratios correlated to Mn valence, 3 only used peaks from L_3 peak, 6 only used peaks from L_2 peak, and 3 used peaks from L_3 and L_2 peaks. Among them, we prefer those using peaks common to several valences and major peaks. Two correlations are therefore selected as calibration. The selected spectral parameter in the first calibration is a ratio between the intensities at two energy points of the L_2-edge, i.e. at L_2-a in Mn^{2+} spectra (651.7 eV) and at the L_2-e major peak in Mn^{4+} spectra (655.2 eV). The spectral parameter is then expressed as follows:

$$R_{L_2} = \frac{I(at\ 655.2\ eV)}{I(at\ 651.7\ eV)}$$

From this parameter, the first calibration equation is (Figure 4a):

$$Mn\ mean\ valence = \frac{R_{L_2} + 6.705}{3.512} \quad (2)$$

It shows a coefficient of determination (R^2) of 0.999. The same R_{L2} value is obtained for ardennite and rhodonite (and jacobsite, not used for calibration), showing that R^2 is not influenced by the Mn atomic environment but only by the Mn valence. This perfect correlation can be used to map Mn valence on unknown samples, since only two images (at fixed energy, i.e. 651.7 and 655.2 eV) are required.

The spectral parameter defined in the second calibration is the ratio between the intensity at L_3-egde energy point (i.e. 641.6 eV, the energy position of the L_3-b major peak of Mn^{2+} spectra) and the intensity at L_2-edge energy point (i.e. 655.2 eV, the energy position of the L_2-e major peak of Mn^{4+} spectra). The calibration equation is expressed as follows (Figure 4b):

$$Mn\ mean\ valence = \frac{R_{L_{2,3}} + 0.669}{0.386} \quad (3)$$

with

$$R_{L_{2,3}} = \frac{I(at\ 655.2\ eV)}{I(at\ 641.6\ eV)}$$

The coefficient of determination for this second calibration (R^2) is 0.984, slightly lower than the one of the first calibration. The difference between $R_{L2,3}$ values for rhodonite and ardennite (and jacobsite) suggests a contribution of Mn atomic environment in addition to the Mn valence dependence. However, taking an intensity on the L_3-edge (which is more intense

than the L_2) and one on the L_2-edge improves the signal to noise ratio. As for the first correlation proposed, the construction of a Mn valence map from STXM-XANES data is made possible by equation 3.

3.3. STXM-XANES coupling: Mn redox mapping

The scanning properties of the microscope allow to record a stack of 125 energy images over the 635-660 eV with a spectral resolution of 0.2 eV. Equations 2 and 3 permit the Mn mean valence to be estimated from the spectrum intensities at two energies. This gives the possibility to easily map the Mn valence from two energy images, and use one of the two calibrations proposed.

In fact, two other XANES images are required in addition to the two images used for mapping, in order to subtract the background at each pixel of the images. Therefore, only four energy images should be selected to calculate the *R* parameter. In the Figure 5, the calibration procedure that uses the equation 3 and the $R_{L2,3}$ parameter is drawn as example (piemontite sample). It is obtained by extracting one image at 641.6 eV, one at 655.2 eV, one in the pre-edge (to apply the ‘‘linear background correction’’ at each pixel of the 641.6 eV image), and one beyond the energy corresponding to the L_2 peak (to remove the linear background and the second edge step of the arctan function at each pixel of the 655.2 eV image). The ratio of corrected 641.6 and 655.2 eV images can then be used to determine the $R_{L2,3}$ for each pixel and to obtain the map of Mn redox state. In this way, the linear background is represented by only one energy at one energy position, so this point should be fairly close to the first peak (638 eV in Figure 5). In the case of spectra with a strong background noise, it is possible to make an “image average” (giving an average value of the linear pre-peak background) by selecting about 10 images between 625 and 639 eV, by adding them and then by dividing the resulting “image sum" by 10 thanks to the aXis2000 software.

If the equation 2 is chosen for calibration, the images required to calculate the R_{L2} parameter need to be selected at 651.7 eV (L_2-a), at 655.6 eV (L_2-e), at the inflexion point

between the L_3 peak and the L_2 peak (to remove the background from the 651.7 eV), and one beyond the L_2 peak (to remove the linear background and the second edge step of the arctan function for each pixel of the 655.2 eV image). By applying the same procedure as before, the Mn map can be reconstructed only from the L_2-edge data.

Resulting quantitative Mn redox maps are a useful tool to identify the Mn mean valence of unknown nanometric particles, but have some limitations. On a map built from $R_{L2,3}$ parameter for a no-pure piemontite sample constructed with equation 3 (Figure 6), the Mn-free crystallites appear in white (Figure 5G and Figure 6) while in areas where the particle is too thick and/or highly concentrated in Mn, valence is overestimated (Figure 6B). In the first case, the absence of Mn leads to calculate the ratio between two too weak absorption pixels (Figure 5E and F). In the second case, a too high X-ray absorption cause an absorption saturation of the L_3 peak, which is more intense than the L_2 peak. This phenomenon generates a nonlinear response of the absorption detection, artificially modifying the relative peak intensities, affecting the $R_{L2,3}$ calculation and overestimating the Mn valence. Although more sensitive to the signal/noise ratio, the use of the R_{L2} parameter and equation 2 to map the Mn valence, based exclusively on the L_2 peak, may provide a favourable way to circumvent absorption saturation issues encountered with the L_3 peak (Figure 6C).

The spatial averaging effect of the X-ray beam over the pixel size (i.e., 40 nm) must also be taking into account. This effect fixes the limit of the minimum distance over which phase contacts or phase rims can be discriminated.

Surpassing these limitations easily identifiable, the STXM-based XANES quantitative map becomes a precise tool, giving an estimate of Mn valence with a high spatial resolution, as demonstrated by the map of piemontite in the Figure 6.

3.4. Assessment of saturation and beam damage effects

Although EELS is known to cause more damage than STXM on the structure of minerals (e.g. de Groot et al. 2010), the latter is nonetheless a method that damages particles

400 during analysis if precautions are not taken. Potentially, the repeated scan of particles at each
401 energy point of a spectrum can altered the structure of the crystallites, and consequently the
402 Mn mean valence estimate. A stack recorded on a 5x5 µm area, obtained with a spatial
403 resolution of 50 nm, a spectral resolution of 0.2 eV and a dwell time of 5 ms per energy- and
404 image- point results in a total analysis time of 2.5 hours (dead time excluded) and of 0.875 s
405 per image-point. To evaluate beam damages, spectral changes at the Mn $L_{2,3}$-edges were
406 monitored with increasing dwell times, from 1 to 20 ms per energy- and image- point. The
407 resulting XANES spectra do not show significant changes, while R_{L2} and $R_{L2,3}$ parameters are
408 only slightly affected, varying by less than 5%. Consequently, the effect of beam damages on
409 the Mn valence estimate is negligible in the typical dwell time range used during routine
410 analyses.

411 The saturation of spectrum can also alter assessment of R_{L2} and $R_{L2,3}$ parameters (see
412 section 3.3). This phenomenon occurs when particles are too thick or too rich in Mn (or a
413 combination of both), leading to a distortion of the spectrum. Hanhan et al. (2009) for Ca and
414 Bourdelle et al. (2013) for Fe proposed to evaluate the maximum intensity of the major peak
415 not to be exceeded to avoid saturation effect. Applying a similar approach, the maximum Mn
416 L_3 peak intensity, below which the L_3/L_2 peak intensity ratio varies linearly and the spectrum
417 is undistorted, was determined. For this, a stack was recorded on a powder of piemontite
418 sample (Mn^{3+}) with particles of various thicknesses. Figure 7 plots the intensity of the L_3
419 major peak according to the one of L_2 major peak for each image-point. The intensities of
420 these two peaks increase linearly until ~0.25 OD. When the particle is thick enough for the L_3
421 major peak intensity to exceed 0.25 OD, the L_3/L_2 intensity ratio no longer evolves linearly,
422 i.e. the intensity of L_2 major peak increases faster than that of L_3 major peak, reflecting the
423 spectra distortion for the considered image-points. This observation is also valid for Mn^{2+} and
424 Mn^{4+} spectra. Consequently, all the quantitative data in this study were therefore obtained
425 from areas presenting a L_3 major peak intensity lower than 0.25 OD. It should be noted that
426 Mn is much more sensitive to saturation phenomena than Fe (saturation effects at > 1.5 OD at

the Fe $L_{2,3}$-edges; Bourdelle et al. 2013), i.e. saturation effects appear at relatively low Mn content (concentration or weak sample thickness). On an indicative basis, piemontite, which is a phase that is not very rich in Mn, presents saturated spectra for a crystallite thickness higher than ~150 nm, while Mn-rich jacobsite shows saturation effects on spectrum when crystallite thickness is around 70 nm.

The crystal orientation compared with the direction of polarisation of the X-ray beam may also influence the spectrum shape. This process is called linear dichroism (Benzerara et al. 2011), and can be thwart using a circular polarized beam as here. The residual dichroism effect was evaluated by comparing spectra from different piemontite particles with various orientation. No change in spectrum shape was observed, and the impact of particle orientation on the Mn mean valence estimate remained undetectable.

5. Conclusion

In the present work, we explore the possibility to construct quantitative Mn redox maps for silicates using the STXM coupled with XANES spectroscopy at the Mn $L_{2,3}$-edges. With fairly limited precautions, we demonstrate that this type of maps could be obtained from two easy-to-use empirical calibrations linking the Mn mean valence to a simple ratio of intensities from selected energy positions. We applied this approach on a mix of piemontite and no-Mn phase sample, demonstrating the potential of it to assess the Mn valence at the nanoscale through micrometric areas. Even if calibrations and map construction have yet to be tested on silicates containing Mn under several oxidation states, as Mn-phyllosilicates, these results pave the way for the study of nanochemical zonations in heterogeneous silicates.

Acknowledgements

We are most grateful to the PSI SLS synchrotron, especially Benjamin Watts (PolLux beamline) for technical advice. Thanks are extended to Philippe Recourt (LOG, Univ. Lille) for sample preparation and to Francis Coune for providing ardennite sample. The authors

wish also to thank the editor and the two anonymous reviewers for comments and suggestions that improved the paper. This study was financially supported by LGCgE.

References

Albee AL, Chodos AA (1970) Semiquantitaive electron microscope determination of Fe2+/Fe3+ and Mn2+/Mn3+ in oxides and silicates and its application to petrologic problems. Am Mineral 55:491-501.

Benzerara K, Menguy N, Obst M, Stolarski J, Mazur M, Tylisczak T, Brown GE Jr, Meibom A (2011) Study of the crystallographic architecture of corals at the nanoscale by scanning transmission X-ray microscopy and transmission electron microscopy. Ultramicroscopy 111:1268–1275

Bobos I, Noronha F, Mateus A (2018) Fe-, Fe,Mn- and Fe,Mg-chlorite: a genetic linkage to W, (Cu, Mo) mineralization in the magmatic-hydrothermal system at Borralha, northern Portugal. Mineral Mag 82:S259-S279

Bosi F, Biagioni C, Pasero M (2019) Nomenclature and classification of the spinel supergroup. Eur J Mineral 31:183-192

Bourdelle F, Beyssac O, Parra T, Chopin C (2018) Nanoscale chemical zoning of chlorite and implications for low-temperature thermometry: Application to the Glarus Alps (Switzerland). Lithos 314:551-561

Bourdelle F, Benzerara K, Beyssac O, Cosmidis J, Neuville DR, Brown GE, Paineau E (2013) Quantification of the ferric/ferrous iron ratio in silicates by scanning transmission X-ray microscopy at the Fe L-2,L-3 edges. Contrib Mineral Petrol 166:423-434

Brotton SJ, Shapiro R, van der Laan G, Guo J, Glans PA, Ajello JM (2007) Valence state fossils in Proterozoic stromatolites by L-edge X-ray absorption spectroscopy. J Geophys Res Biogeosci 112:G3

Burns R (1993) Mineralogical Applications of Crystal Field Theory (Cambridge Topics in Mineral Physics and Chemistry). Cambridge: Cambridge University Press. doi:10.1017/CBO9780511524899

Chen CT, Idzerda YU, Lin HJ, Smith NV, Meigs G, Chaban E, Ho GH, Pellegrin E, Sette F (1995) Experimental confirmation of the X-ray magnetic circular-dichroism sum-rules for iron and cobalt. Phys Rev Lett 75:152–155

Cuartero V, Lafuerza S, Rovezzi M, Garcia J, Blasco J, Subias G, Jiménez E (2016) X-ray absorption and emission spectroscopy study of Mn and Co valence and spin states in $TbMn_{1-x}Co_xO_3$. Phys rev B 94:155117

de Groot FMF, de Smit E, van Schooneveld MM, Aramburo LR, Weckhuysen BM (2010) In-situ scanning transmission X-ray microscopy of catalytic solids and related nanomaterials. Chem Phys Chem 11:951–962

de Groot FMF (1994) X-ray absorption and dichroism of transition metals and their compounds. J Electron Spectros Relat Phenomena 67:529-622

Donnay G, Allmann R (1968) Si3O10 Groups in the Crystal Structure of Ardennite. Acta Cryst B 24:845

Garvie LAJ, Craven AJ (1994) High-resolution parallel electron energy-loss spectroscopy of Mn L2,3-edges in inorganic manganese compounds. Phys Chem Miner 21:191-206

Garvie LAJ, Craven AJ, Brydson R (1994) Use of electron-energy loss near-edge fine structure in the study of minerals. Am Mineral 79:411-425

Hanhan S, Smith AM, Obst M, Hitchcock AP (2009) Optimization of analysis of soft X-ray spectromicroscopy at the Ca 2p edge. *J* Electron Spectros 173:44–49

Hitchcock AP (2012) aXis 2000 analysis of X-ray images and spectra. McMaster University, Hamilton

Ilton ES, Post JE, Heaney PJ, Ling FT, Kerisit SN (2016) XPS determination of Mn oxidation states in Mn (hydr)oxides. Appl Surf Sci 366:475–485

505 Inoue A, Inoue S, Utada M (2018) Application of chlorite thermometry to estimation of
506 formation temperature and redox conditions. Clay Miner 53:143–158
507 Kubin M, Guo M, Kroll T, Löchel H, Källman E, Baker ML, Mitzner R, Gul S, Kern J,
508 Föhlisch A, Erko A, Bergmann U, Yachandra V, Yano J, Lundberg M, Wernet P (2018)
509 Probing the oxidation state of transition metal complexes: a case study on how charge and
510 spin densities determine Mn L-edge X-ray absorption energies. Chem Sci 9:6813
511 Lauterbach S, McCammon CA, van Aken P, Langenhorst F, Seifert F (2000) Mossbauer and
512 ELNES spectroscopy of (Mg, Fe)(Si,Al)O3 perovskite: a highly oxidised component of the
513 lower mantle. Contrib Mineral Petrol 138:17–26
514 Livi KJT, Lafferty B, Zhu M, Zhang S, Gaillot A-C, Sparks DL (2012) Electron Energy-Loss
515 Safe-Dose Limits for Manganese Valence Measurements in Environmentally Relevant
516 Manganese Oxides. Environ Sci Technol 46:970−976
517 Loomer D, Al T, Weaver L, Cogswell S (2007) Manganese valence imaging in Mn minerals
518 at the nanoscale using STEM-EELS. Am Mineral 92:72-79
519 Manceau A, Gallup DL (2005) Nanometer-sized divalent manganese-hydrous silicate
520 domains in geothermal brine precipitates. Am Mineral 90:371-381
521 Manceau A, Marcus MA, Grangeon S (2012) Determination of Mn valence states in mixed-
522 valent manganates by XANES spectroscopy. Am Mineral 97:816–827
523 Morales F, de Groot FMF, Glatzel P, Kleimenov E, Bluhm H, Hävecker M, Knop-Gericke A,
524 Weckhuysen BM (2004) In Situ X-ray Absorption of Co/Mn/TiO2 Catalysts for Fischer-
525 Tropsch Synthesis. J Phys Chem B 108:16201-16207
526 Nagashima M, Armbruster T (2010) Ardennite, tiragalloite and medaite: structural control of
527 (As5+, V5+, Si4+)O4 tetrahedra in silicates. Mineral Mag 74:55–71
528 Nelson WR, Griffen DT (2005) Crystal chemistry of Zn-rich rhodonite ("fowlerite"). Am
529 Mineral 90:969-983

Nishida S, Kobayashi S, Kumamoto A, Ikeno H, Mizoguchi T, Tanaka I, Ikuhara Y, Yamamoto T (2013) Effect of local coordination of Mn on Mn-L2,3 edge electron energy loss spectrum. J Appl Phys 114:054906

Pecher K, McCubbery D, Kneedler E, Rothe J, Bargar J, Meigs G, Cox L, Nealson K, Tonner B (2003) Quantitative charge state analysis of manganese biominerals in aqueous suspension using Scanning Transmission X-ray Microscopy (STXM). Geochim Cosmochim Acta 67:1089–1098

Pérez-Dieste V, Crain J N, Kirakosian A, McChesney J L, Arenholz E, Young A T, Denlinger J D, Ederer D L, Callcott T A, Lopez-Rivera S A, Himpsel FJ (2004) Unoccupied orbitals of 3d transition metals in ZnS. Phys Rev B 70:085205

Raabe J, Tzvetkov G, Flechsig U, Böge M, Jaggi A, Sarafimov B, Vernooij MGC, Huthwelker T, Ade H, Kilcoyne D, Tyliszczak T, Fink RH, Quitmann C (2008) PolLux: A new facility for soft X-ray spectromicroscopy at the Swiss Light Source. Rev Sci Instrum 79

Risch M, Stoerzinger KA, Han B, Regier TZ, Peak D, Sayed SY, Wei C, Xu Z, Shao-Horn Y (2017) Redox Processes of Manganese Oxide in Catalyzing Oxygen Evolution and Reduction: An in Situ Soft X‑ray Absorption Spectroscopy Study. J Phys Chem C 121:17682−17692

Smyth JR, Bish D L (1988) Crystal Structures and Cation Sites of the Rock-Forming Minerals London and Boston (Unwin-Hyman Ltd.). Mineral Mag 52:733-734

Sussenberger A, Pospiech S, Schmidt ST (2018) [MnO vertical bar SiO2, Al2O3, FeO, MgO] balanced log-ratio in chlorites: a tool for chemo-stratigraphic mapping and proxy for the depositional environment. 16th International Clay Conference (ICC) Location: Granada. Clay miner 53:351-375

Tan H, Verbeeck J, Abakumov A, van Tendeloo G (2012) Oxidation state and chemical shift investigation in transition metal oxides by EELS. Ultramicroscopy 116:24–33

van Aken PA, Liebscher B (2002) Quantification of ferrous/ferric ratios in minerals: new evaluation schemes of Fe L-23 electron energy-loss near-edge spectra. Phys Chem Miner 29:188–200

Van der Laan G, Kirkman IW (1992) The 2p absorption spectra of 3d transition metal compounds in tetrahedral and octahedral symmetry. J Phys: Condens Matter 4:4189-4204

Wang H, Friedrich S, Li L, Mao Z, Ge P, Balasubramanian M, Patil DS (2018) L-edge sum rule analysis on 3d transition metal sites: from d10 to d0 and towards application to extremely dilute metallo-enzymes. Phys Chem Chem Phys 20:8166–8176

Zhang S, Livi KJT, Gaillot A-C, Stone AT, Veblen DR (2010) Determination of manganese valence states in (Mn3+, Mn4+) minerals by electron energy-loss spectroscopy. Am Mineral 95:1741–1746

Figure captions

Fig. 1 Representative XANES spectra at the Mn $L_{2,3}$-edges for the Mn-silicates and jacobsite. The spectra have been normalised to the major L_3 peak intensity, and some of the spectra have been shifted vertically for clarity (normalised intensity with arbitrary units). The vertical lines indicate major peaks (solid lines) and minor peaks (dashed lines). Each peak is indexed, redox states and core-excited final state configurations are mentioned

Fig. 2 Focus on L_3-edge for Mn^{2+} phases (rhodonite, ardennite, jacobsite). The spectra have been normalised to the major L_3 peak intensity. Coordination (number of O ligands and sites) is specified for each phases

Fig. 3 L_3-edge center of gravity from XANES spectra versus Mn valence for the selected silicates. Error bars represent the standard deviation calculated on the base of 4 or 5 spectra for each sample. Value for jacobsite is given for information, but not taken into account for calibration calculation

584 **Fig. 4** $L_{2,3}$-edge intensity ratio from XANES spectra versus Mn valence for the selected silicates. (A)
585 R_{L2} ratio, using selected intensities at two energy points (i.e. 651.7 and 655.2 eV) of the L_2-edge. (B)
586 $R_{L2,3}$ ratio, using selected intensities at one energy point (i.e. 641.6 eV) of the L_3-edge and one energy
587 point (i.e. 655.2 eV) of the L_2-edge. Error bars represent the standard deviation calculated on the base
588 of 4 or 5 spectra for each sample, i.e. 18 spectra in total. Values for jacobsite are given for
589 information, but not taken into account for calibration calculation
590
591 **Fig. 5** Determination of the Mn valence from 4 selected energy images: one image in the pre-edge (to
592 apply the ‘‘linear background correction’’ at each pixel of the image; image A), one at 641.6 eV (L_3-b
593 major peak of Mn^{2+}; image B), one at 655.2 eV (L_2-e major peak of Mn^{4+}; image C) and one beyond
594 the L_2-edge (to remove the edge step of the arctan function; image D). Finally, the ratio of the
595 resulting 641.6 and 655.2 eV images (E and F) can be used to determine the $R_{L2,3}$ parameter at each
596 pixel of the image and obtain Mn redox mapping (G). All images are OD images, where piemontite
597 and no Mn-silicate are the light-grey and dark phases on image E, respectively. White scale: 1 µm
598
599 **Fig. 6** Quantitative Mn redox nanomapping on particles from no-pure piemontite sample. A: optical
600 density image at 641.6 eV, where the piemontite and no-Mn silicate particles are the light-grey and
601 white phases, respectively. B: manganese redox mapping, calculated from the $R_{L2,3}$ parameter coupled
602 with the Eq. (3). C: manganese redox mapping, calculated from the R_{L2} parameter coupled with the Eq.
603 (2). The spatial averaging effect of the X-ray beam over the pixel size (i.e., 40 nm) sets the limit of the
604 minimum distance (turquoise rims, underlined by a yellow square). No-Mn silicates, identified by blue
605 dashed polygon on the OD image, appear in white on the redox map B and in black for no Mn
606 absorption on the redox map C and image E of the Fig. 5. Areas where the particle thickness is too
607 high to obtain no-saturated images (see section 3.4.) – highlighted by a purple polygon on the OD
608 image – lead to the overestimate of Mn valence (pink and red zones of the redox map B), up to the
609 total saturation (appearing in white on the map). Areas presenting no-too-thick piemontite particles
610 (i.e. the rest of the OD image) appear in blue on the Mn redox maps, testifying of trivalent manganese
611

612 **Fig. 7** Difference, pixel by pixel, of intensity detected between the L_3 major peak and the L_2 major
613 peak images (in which a pre-edge image was subtracted) for a no-pure piemontite sample (4661
614 pixels). The dashed line was calculated from a quadratic equation. Insets: representative spectra and
615 optical density image (641.6 eV) for a no-pure piemontite sample

Figure1

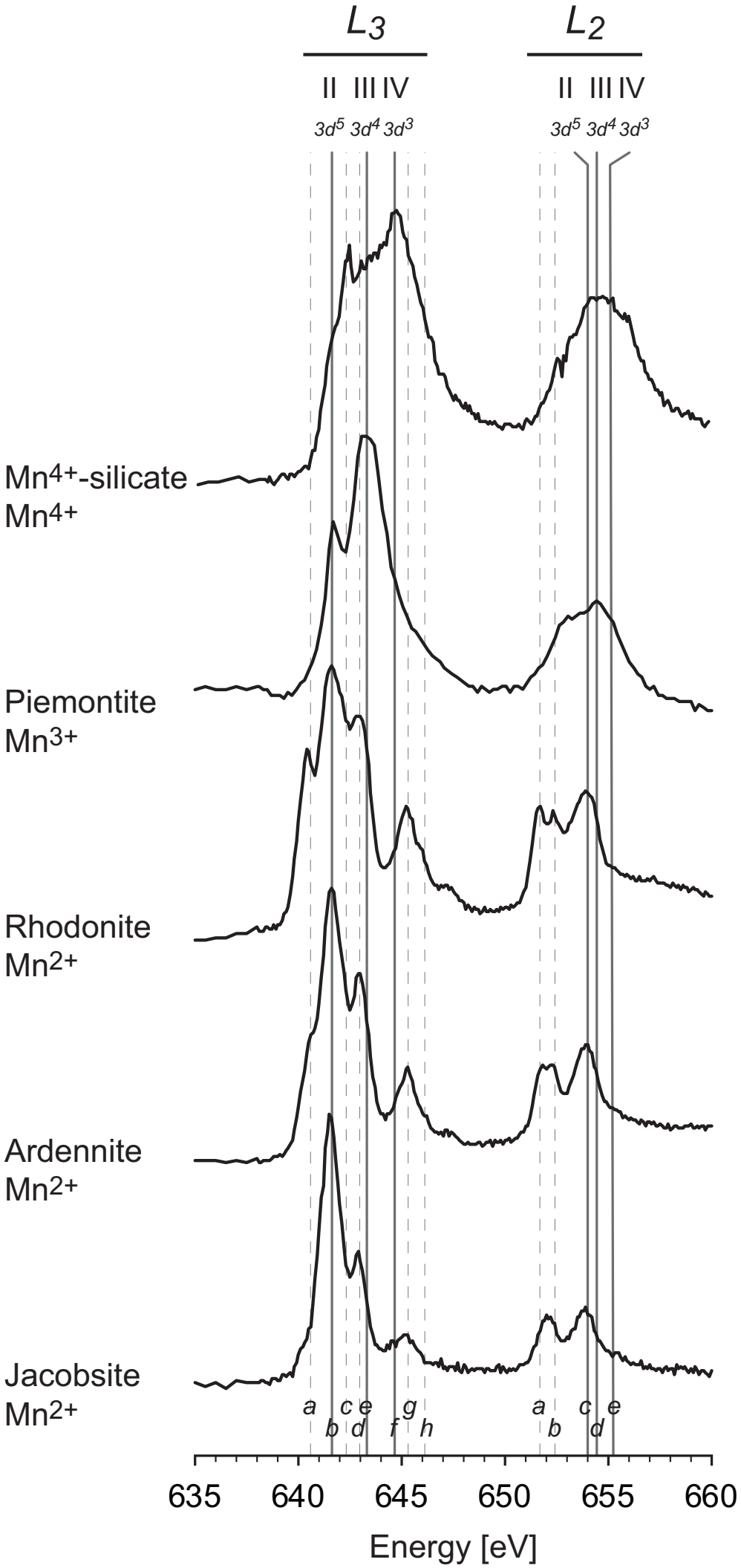
L3
L2
II III IV
II III IV
3d5 3d4 3d3
3d5 3d4 3d3
Mn4+-silicate
Mn4+
Piemontite
Mn3+
Rhodonite
Mn2+
Ardennite
Mn2+
Jacobsite
Mn2+
a b c d e f g h
a b c d e
635 640 645 650 655 660
Energy [eV]

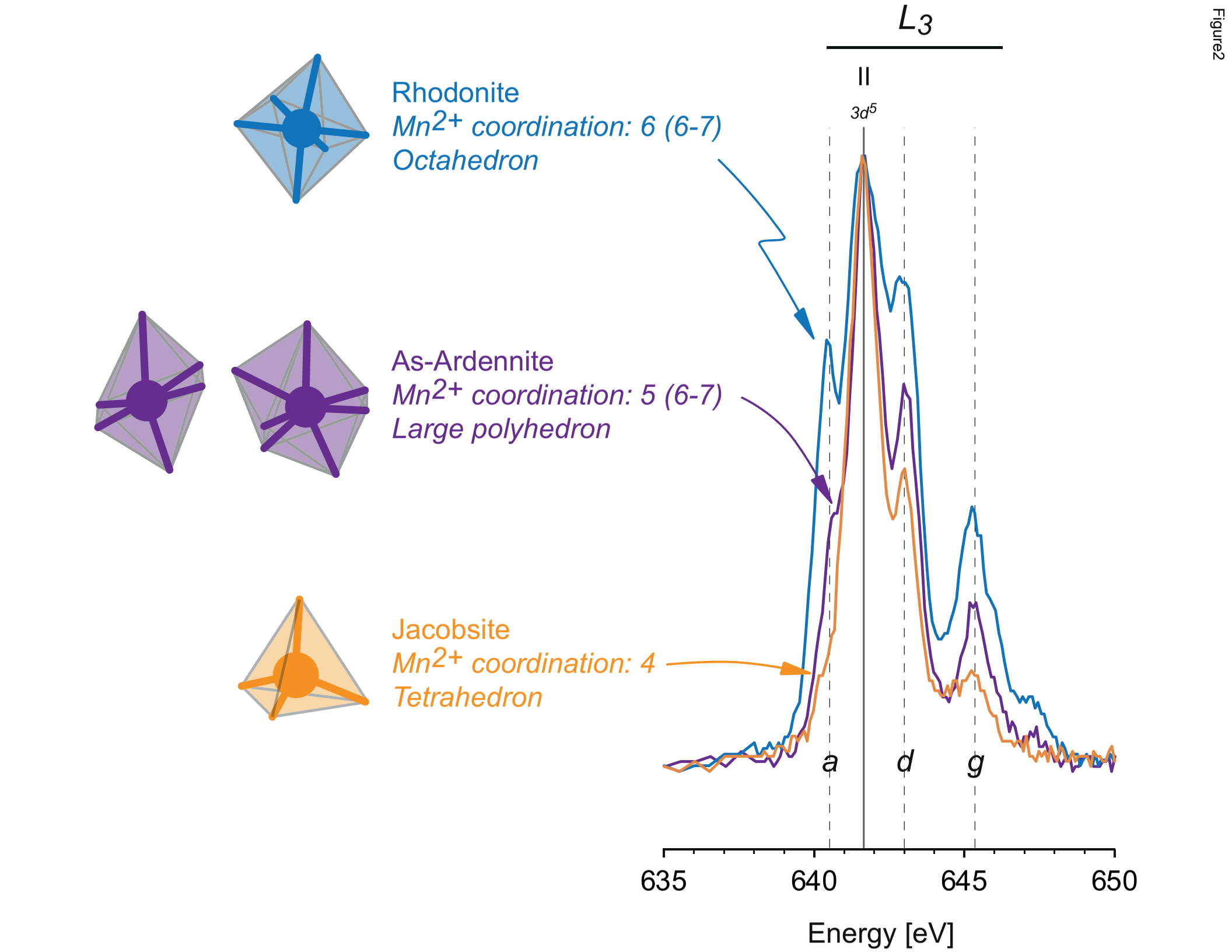
Figure2
Rhodonite
Mn2+ coordination: 6 (6-7)
Octahedron
As-Ardennite
Mn2+ coordination: 5 (6-7)
Large polyhedron
Jacobsite
Mn2+ coordination: 4
Tetrahedron
L3
II
3d5
a
d
g
635
640
645
650
Energy [eV]

Figure3

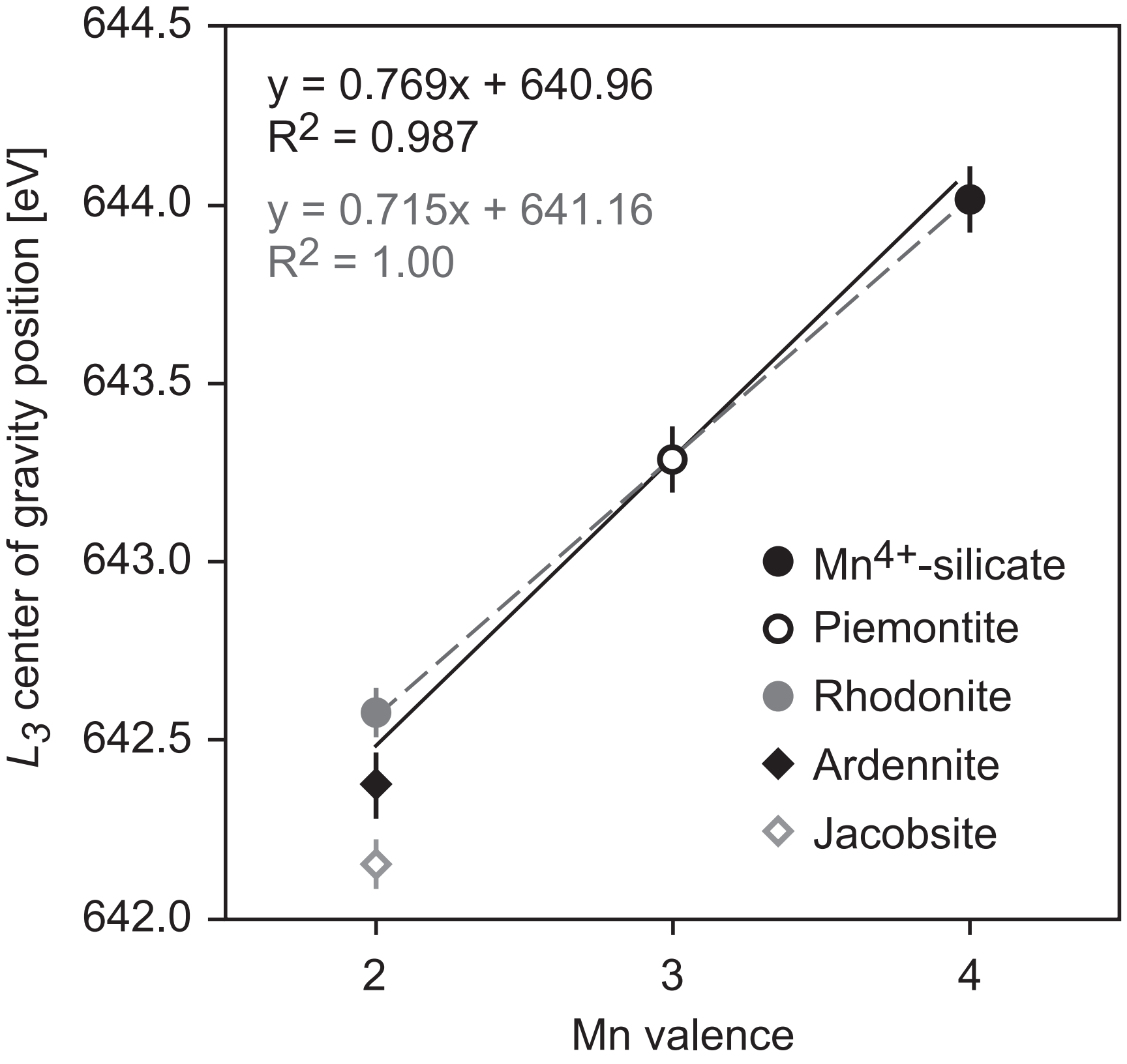
644.5
644.0
643.5
643.0
642.5
642.0
L_3 center of gravity position [eV]
y = 0.769x + 640.96
R^2 = 0.987
y = 0.715x + 641.16
R^2 = 1.00
Mn^{4+}-silicate
Piemontite
Rhodonite
Ardennite
Jacobsite
2
3
4
Mn valence

Figure4

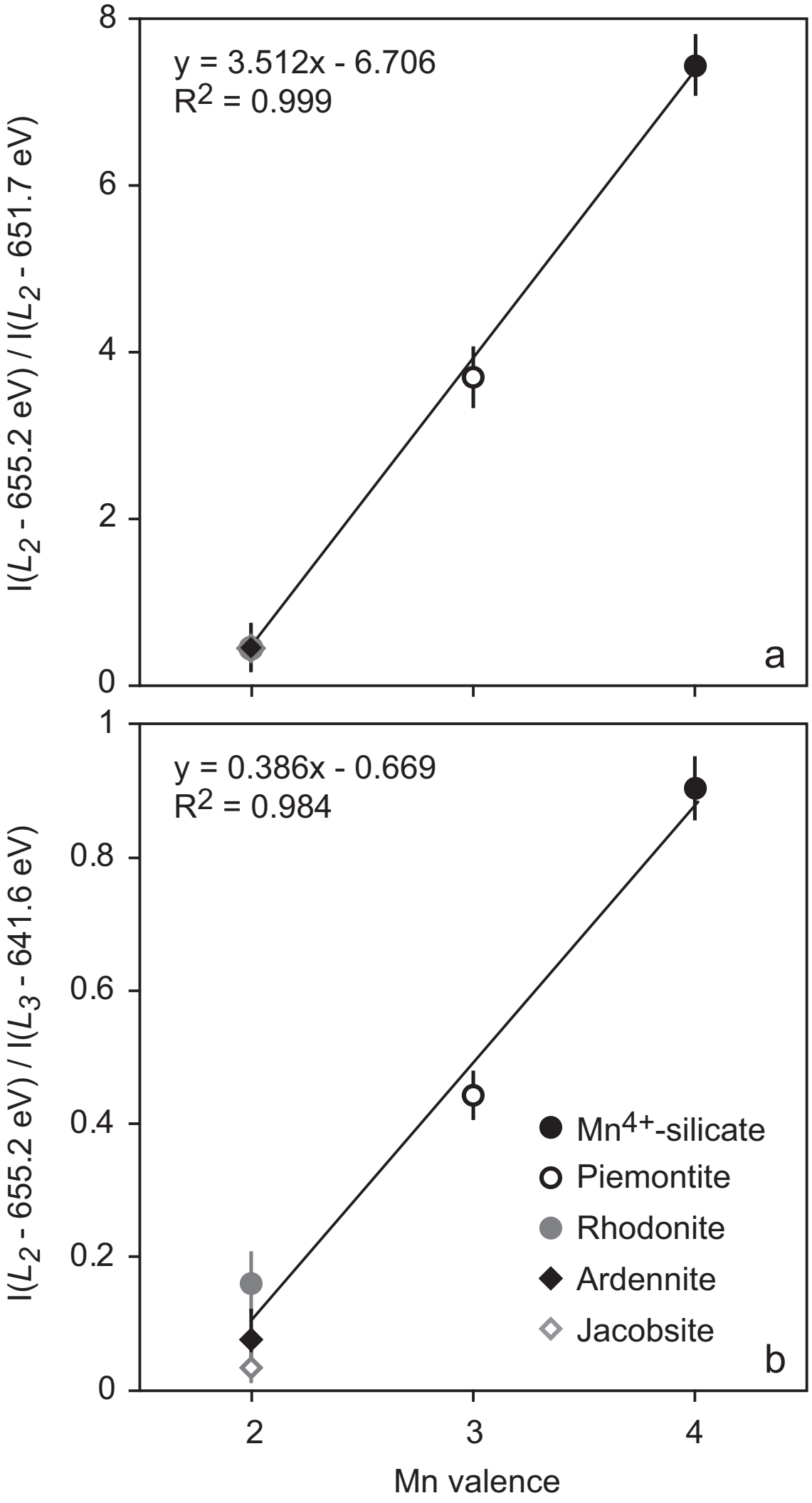
y = 3.512x - 6.706
R2 = 0.999
I(L2 - 655.2 eV) / I(L2 - 651.7 eV)
a
y = 0.386x - 0.669
R2 = 0.984
I(L2 - 655.2 eV) / I(L3 - 641.6 eV)
Mn4+-silicate
Piemontite
Rhodonite
Ardennite
Jacobsite
b
Mn valence

Figure5

Click here to access/download;Figure;Fig5.tif

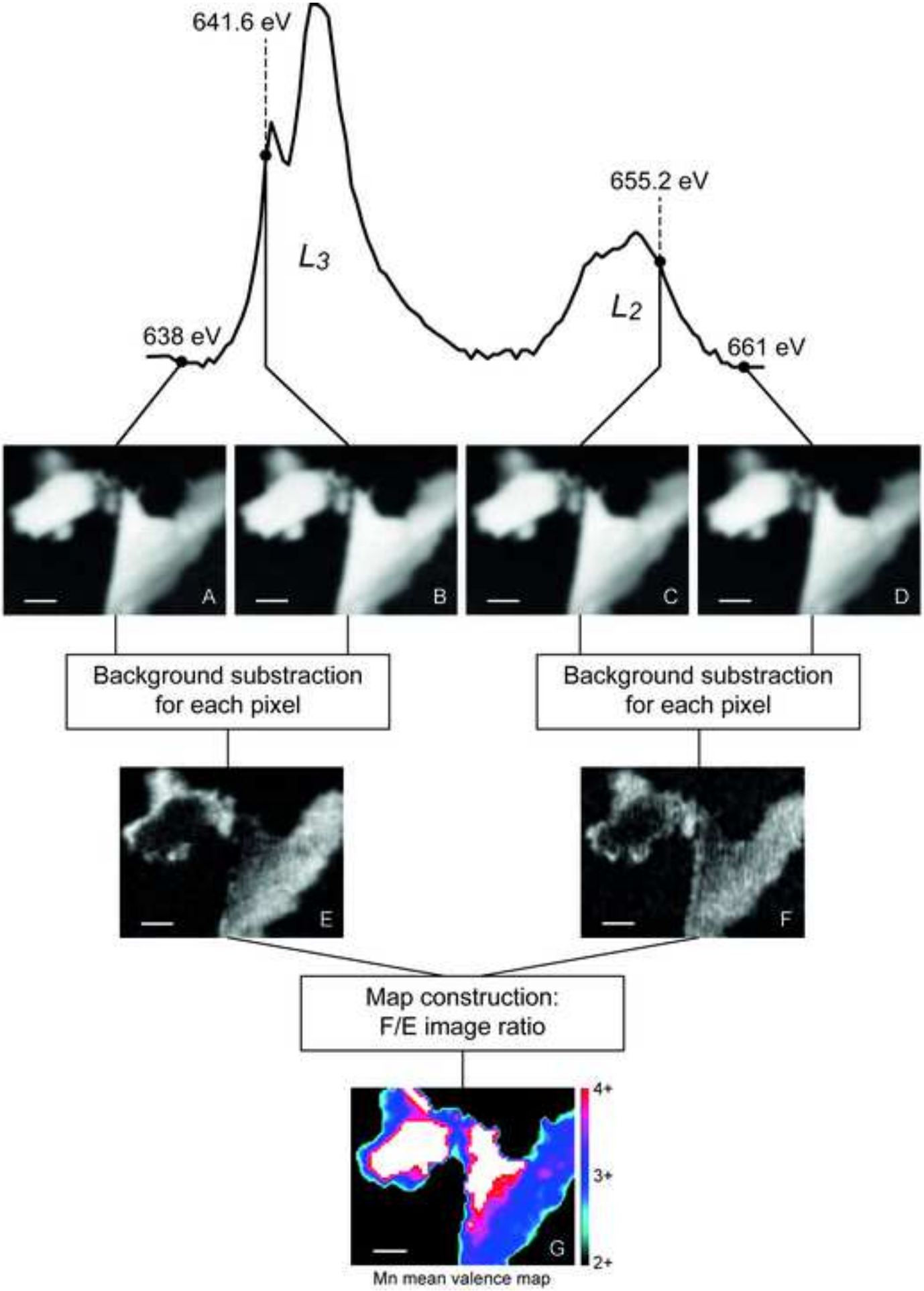

Figure6

Click here to access/download;Figure;Fig6.tif

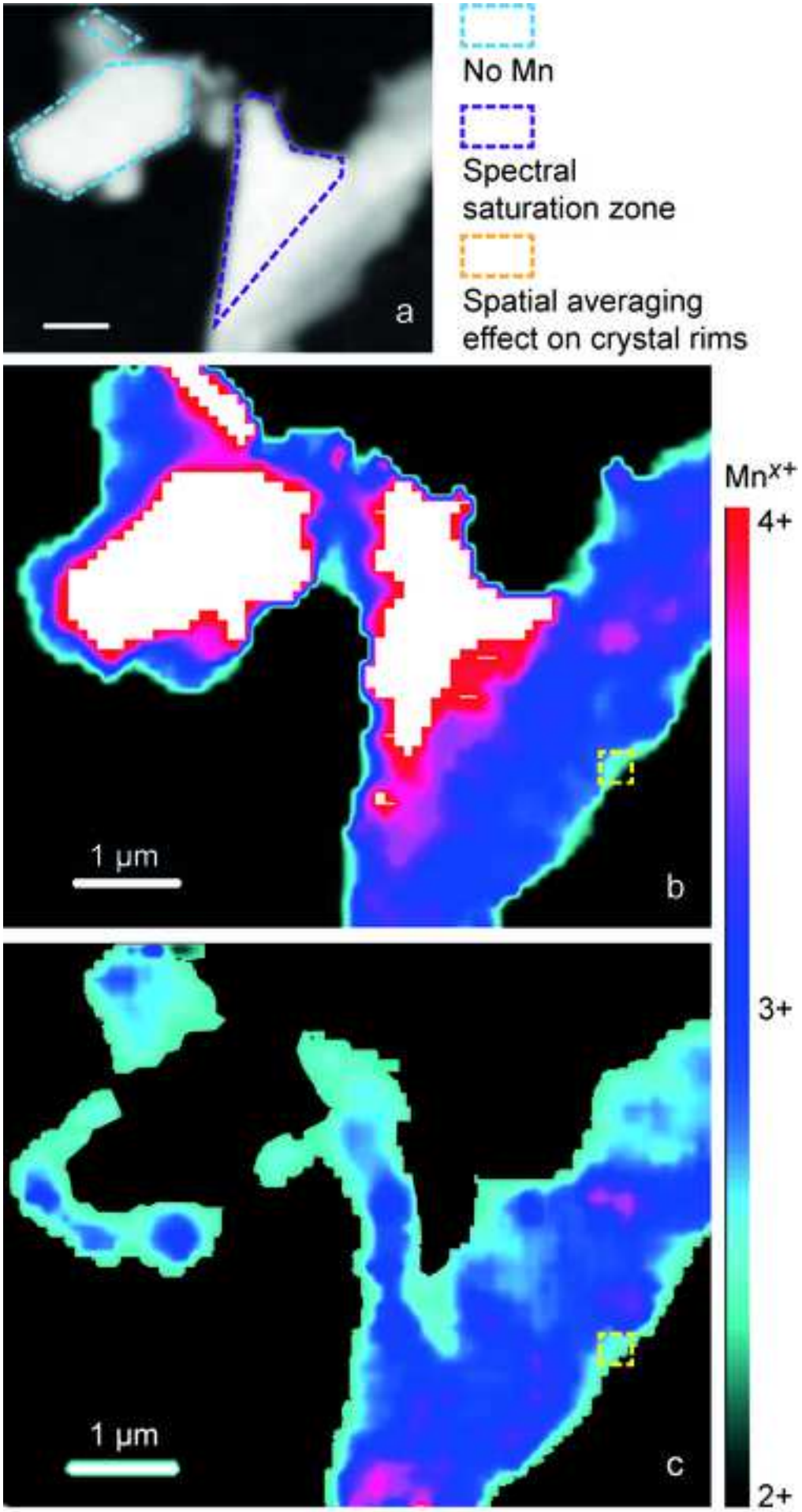

Figure7

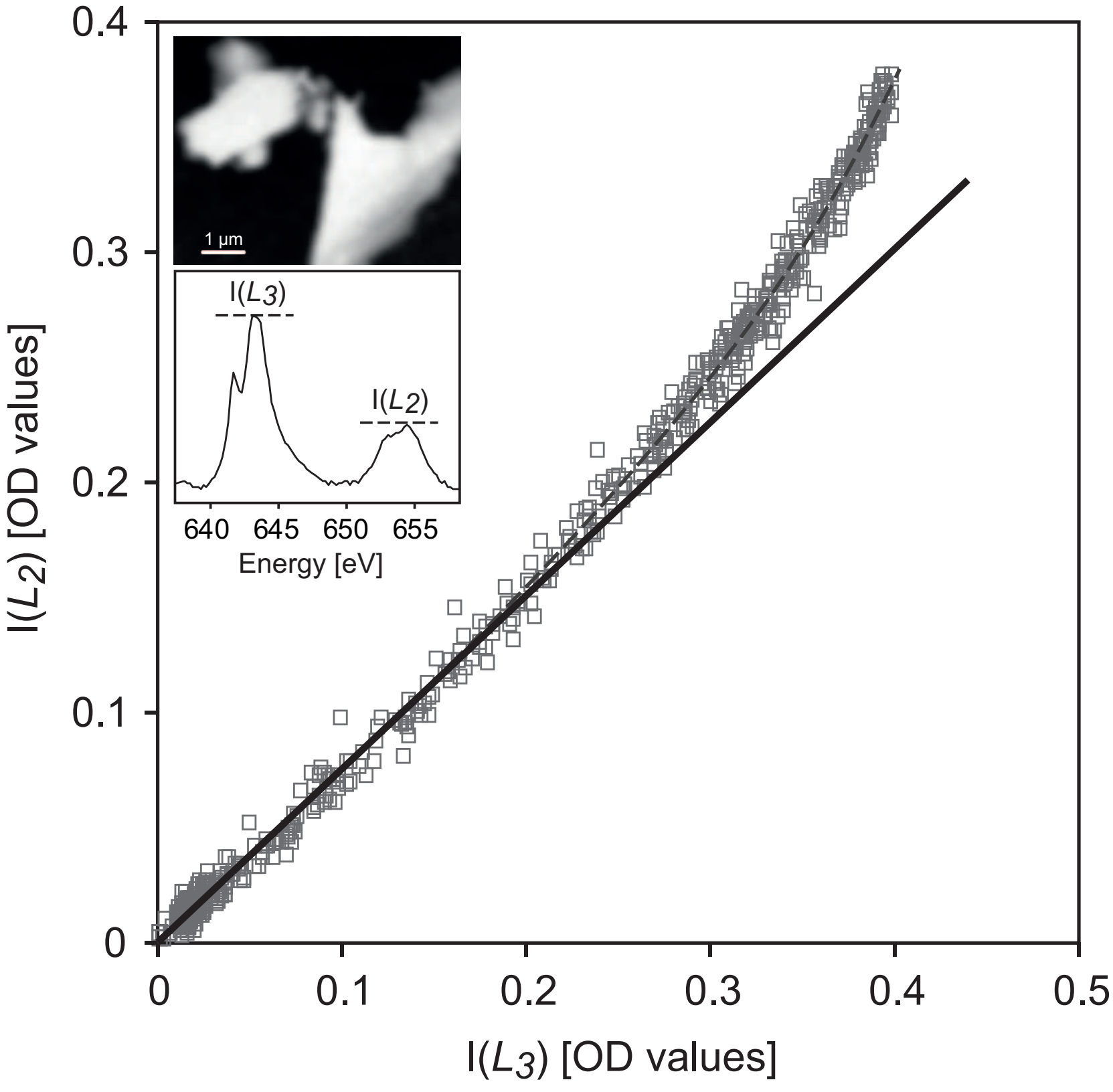
0.4
0.3
0.2
0.1
0
0
0.1
0.2
0.3
0.4
0.5
I(L2) [OD values]
I(L3) [OD values]
1 µm
I(L3)
I(L2)
640
645
650
655
Energy [eV]